Journal of Computational Physics 488 (2023) 112232

Contents lists available at ScienceDirect

Journal of Computational Physics

journal homepage: www.elsevier.com/locate/jcp

A combined immersed finite element and conservative semi-Lagrangian scheme for plasma-material interactions

Hongtao Liu [a,b], Mengyu Chen [a], Xiaofeng Cai [c,d,*], Yong Cao [a,*], Giovanni Lapenta [b]

[a] School of Mechanical Engineering and Automation, Harbin Institute of Technology, Shenzhen, 518055, China
[b] Center for Mathematical Plasma Astrophysics, Department of Mathematics, KU Leuven, Leuven, 3001, Belgium
[c] Research Center for Mathematics, Advanced Institute of Natural Sciences, Beijing Normal University, Zhuhai, 519087, China
[d] Guangdong Provincial Key Laboratory of Interdisciplinary Research and Application for Data Science, BNU-HKBU United International College, Zhuhai, 519087, China

ARTICLE INFO

Article history:
Received 5 December 2022
Received in revised form 11 May 2023
Accepted 13 May 2023
Available online 25 May 2023

Keywords:
Semi-Lagrangian scheme
Immersed finite element
Vlasov-Possion system
Plasma-material interactions

ABSTRACT

In this paper, the immersed finite element (IFE) coupled with the conservative semi-Lagrangian (CSL) kinetic scheme is developed for plasma-material interactions. The proposed method (IFE-CSL) enjoys respective advantages of the IFE and CSL, i.e., the flexibility and efficiency for treating complex boundary conditions, mass conservation and being free from the Courant-Friedrichs-Lewy (CFL) condition. In the current IFE-CSL, the IFE method based on structured interface-independent meshes is developed for the spatial discretization of the field equation, which provides an accurate approach with convenient implementations to solve the field problems with irregular interface. The CSL scheme combined with an immersed method termed half-way ghost-cell is proposed for the spatial discretization of the Vlasov equation, which enables the proposed method to exactly conserve mass and conveniently handle curved boundaries. Then the IFE and CSL method are coupled via the charge density depending on full kinetic or hybrid kinetic model, where the appropriate IFE solver is developed for the linear or nonlinear Poisson equation, respectively. In the current IFE-CSL, different geometries can be treated automatically for both IFE and CSL through the specific geometric information. As a result, the proposed CSL-IFE can be conveniently and efficiently applied to simulate the plasma-material interactions with structured interface-independent meshes. Finally, several numerical experiments are performed to demonstrate the capabilities of the proposed method.

1. Introduction

Plasma-material interactions attract much attention for their important role in the semiconductor industry, space electric propulsion, fusion physics, and so on [1]. In practice, plasma-material interaction problems generally involve objects with complex geometries, thus interface problems between the plasma and objects need to be accurately resolved. The kinetic model is one of the most appropriate models for plasma simulations due to its universality. Unfortunately, the classical

* Corresponding authorS.
E-mail addresses: hongtao.liu@kuleuven.be (H. Liu), 19S053025@stu.hit.edu.cn (M. Chen), xfcai@bnu.edu.cn (X. Cai), yongc@hit.edu.cn (Y. Cao), giovanni.lapenta@kuleuven.be (G. Lapenta).

https://doi.org/10.1016/j.jcp.2023.112232
0021-9991/

numerical schemes based on unstructured meshes are not popular for plasma kinetic simulations due to the high dimensional property of the kinetic model [2]. In contrast, the Cartesian grids make numerical methods efficient and convenient to implement. In this paper, we aim to propose a novel kinetic scheme based on the Cartesian-mesh for plasma-material interactions, which consists of three main components: solving the corresponding Poisson equation for electrostatic field, the Vlasov equation for plasma dynamic, and the interactions of plasma and objects.

In general, the Poisson equation with discontinuous coefficients across the interface should be utilized to describe the electrostatic field problem with complicated interfaces. For the Poisson equation, indeed a vast array of possibilities exists in computational electromagnetism. However, the classical Cartesian-mesh methods have poor accuracy around the complicated interfaces. Several efforts have been devoted to develop suitable Cartesian-mesh methods for the problems involving irregular interfaces, such as the immersed boundary method (IBM) [3], the level set method (LSM) [4], the immersed finite element (IFE) method [5] and so on. Among these methods, we especially focus on the IFE method due to its favorable accuracy, efficiency and flexibility for the plasma kinetic simulations. The IFE method is a finite element method developed to solve the interface problems based on Cartesian meshes, which was introduced by Lin et al. [5], where rectangular elements are used on a two-dimensional (2-D) domain. The method has been extended to 2-D axisymmetric [6] and 3-D problems with tetrahedral elements [7]. In the plasma community, the IFE method coupled with the particle-in-cell (PIC) method has been proposed for plasma simulations [8–10], where the IFE method provides an accurate approach with convenient implementations to solve interface problems based on structured interface-independent meshes on which the PIC method works most efficiently. Recently, the IFE-PIC method for the ion thruster [11,12], hall thruster [13,14], and lunar surface environment [15,16] also has been proposed.

For solving the Vlasov equation, there are two popular approaches: particle-based approach and grid-based approach. The PIC method is the well-known particle-based method, which is widely applied in plasma simulations for its computation economy, especially for high dimensional problems [17–21]. However, the PIC method involves inherent numerical noise. Alternatively, the grid-based method which directly solves the kinetic equation in phase space [22–29] is attracting researchers as the development of the capacity of high-performance computers. We refer to this method as the direct kinetic method (DKM). The DKM can be convenient to achieve high order accuracy so that it allows the study of fine-scale details, e.g., warm plasma dynamics involving a small perturbation amplitude [30–32] and strong particles collision [33,34]. Among DKM schemes, the conservative semi-Lagrangian (CSL) schemes not only can be escaped from the stringent Courant-Friedrichs-Lewy condition but also exactly conserve the mass of system. This paper adopts a CSL scheme with the positivity preserving property [35–37] to solve the Vlasov equation. We refer to [38,39] for more high order CSL schemes. To our best knowledge, up to now, none of proposed CSL scheme has been coupled with IFE method for plasma simulations involving irregular boundary conditions in plasma community.

In addition to the interface problem on the electrostatic field, a suitable physical boundary scheme should be also specified in the Vlasov equation to accurately describe the interactions of plasma and objects. The IBM is considered to be a promising scheme for flows involving complex interfaces, since the solution of the governing equation and the implementation of boundary conditions is decoupled [40]. One type of IBM is to distribute the Lagrangian markers along the solid-fluid boundary, which might lead to some unphysical phenomena may be induced by the diffuse property [41]. Another type of IBM is the sharp interface scheme, e.g., the ghost-cell (GC) method [3], where the information at the solid cell is extrapolated from the neighboring fluid cells and interface. Compared with the first-type IBM [41], the second-type IBM is free from the body force and preserves the distinguishable interface which contributes to the easy enforcement of the boundary conditions. Among various kinds of IBM [2,42,43], we adopt the half-way ghost-cell (HWGC) method [44] for its convenient implementation.

In this study, we present a novel noiseless plasma kinetic solver, namely, IFE-CSL for plasma simulations involving complex boundary conditions, which is based on the IFE method and a positivity-preserving (PP) CSL scheme. More specifically, the IFE method is proposed to evolute the electrostatic field, which makes the proposed method accurately and efficiently resolve the complicated interface problems based on structured interface-independent meshes. The CSL scheme with positivity preserving property is implemented to evolute the Vlasov equation, which enables the proposed method to preserve the favorable conservative property and positivity of the distribution function. Besides, the HWGC method is applied in CSL to conveniently describe the plasma dynamic around plasma-material interactions. Then we bridge the IFE method and CSL scheme with charge density depending on the full kinetic or hybrid kinetic model, where the appropriate IFE solver is developed for the linear or nonlinear Poisson equation, respectively. Finally, we present several numerical experiments to demonstrate the performance of the proposed IFE-CSL.

The rest of the paper is organized as follows. The Vlasov-Poisson (VP) system and its normalization are introduced in Section 2. In Section 3, the IFE method, the CSL scheme, as well as the appropriate coupling of these two solvers for VP system are described in detail. We present the results of numerical studies in Section 4. Finally, a summary is given in Section 5.

2. The Vlasov-Poisson system

In this section, we recall the VP system and its normalization. The evolution of particles can be described by the VP system,

$$\partial_t f_s + \boldsymbol{v}_s \cdot \nabla_{\boldsymbol{x}} f_s + \frac{q_s}{m_s} \boldsymbol{E} \cdot \nabla_{\boldsymbol{v}_s} f_s = 0, \tag{1}$$

$$-\Delta\phi = \frac{q}{\varepsilon}(n_i - n_e),\ n_s = \int f_s dv_s, \tag{2}$$

where $f_s = f(\boldsymbol{x}, \boldsymbol{v}, t)$ is the velocity distribution function for species s (s chooses e for electrons and i plasma ions) moving in d-dimensional velocity space with $\boldsymbol{v}_s = (v_{s1}, \cdots, v_{sd})$ at position $\boldsymbol{x}$ and time t. Here species charge q_s, elementary charge q, mass m_s, plasma number density n_s, permittivity ε are the plasma parameters. Note that the electric field $\boldsymbol{E}$ is obtained from the potential ϕ with $\boldsymbol{E} = -\nabla_{\boldsymbol{x}}\phi$.

Since both ions and electrons dynamic are described by the Vlasov question, the system Eqs. (1) and (2) are also knows as the full kinetic model. However, in some applications, i.e., the solar wind and ion thruster, we mainly focus on the ion dynamic. To reduce the computation cost, one can assume the electron follows the Maxwellian distribution. Then the number density of electron can be obtained by [45]

$$n_e = n_0 \exp\left(\frac{\phi - \phi_0}{k_B T_e}\right), \tag{3}$$

where k_B is the Boltzmann constant, T_e is the electron temperature, n_0 is the reference number density, and ϕ_0 is the reference potential. With the Boltzmann approximation Eq. (3), the Poisson Eq. (2) can be rewritten as

$$-\Delta\phi = \frac{q}{\varepsilon}\left[n_i - n_0 \exp\left(\frac{q(\phi - \phi_0)}{k_B T_e}\right)\right]. \tag{4}$$

Obviously, Eq. (4) is a nonlinear equation, where the iterative method is required. The system Eqs. (1) and (4), where the ions dynamic are described by Vlasov question while electrons are described by fluid Boltzmann approximation are called the hybrid kinetic model.

It is well known that the Debye length λ and the electron plasma frequency ω_p are the characteristic spatial and temporal parameters for electrostatic plasma, which are given by

$$\lambda = \left(\frac{\varepsilon k_B T}{q^2 n}\right)^{1/2},\ \omega_p = \left(\frac{nq^2}{\varepsilon m_e}\right)^{1/2}.$$

In the present paper, the following dimensionless variables are used to normalize the VP system,

$$\begin{aligned} &\bar{x} = \frac{x}{x_0}, \bar{T} = \frac{T}{T_0}, \bar{m} = \frac{m}{m_0}, \bar{n} = \frac{n}{n_0}, \\ &\bar{v} = \frac{v}{v_0},\ \bar{t} = \frac{t}{t_0},\ \bar{f} = \frac{f}{f_0},\ \bar{\phi} = \frac{\phi}{\phi_0}, \end{aligned} \tag{5}$$

where x_0, T_0, m_0 and n_0 are reference length, temperature, mass and number density, which are independent parameters. Besides, we chose the reference velocity $v_0 = \sqrt{2k_B T_0/m_0}$, potential $\phi_0 = 2k_B T_0/q$ and the distribution function $f_0 = n_0/{v_0}^d$. Once the four parameters x_0, T_0, m_0 and n_0 are chosen, the dimensionless VP system will be uniquely determined.

In the current study, we let $T_0 = T_i$, $m_0 = m_i$, $n_0 = n_i$ unless otherwise stated. The reference length x_0 will be given in the specific simulation. Here we define the dimensionless Debye length $\bar{\lambda} = \lambda/x_0$. Accordingly, the dimensionless electron plasma frequency $\bar{\omega}_p = \omega_p t_0 = 1/\bar{\lambda}$. In the rest of paper, all variables are dimensionless unless stated otherwise, but we will drop the bar over the variables for simplicity. Then the dimensionless VP system (1) and (2) can be written as

$$\partial_t f_s + \boldsymbol{v}_s \cdot \nabla_{\boldsymbol{x}} f_s + \frac{q_s}{m_s} \boldsymbol{E} \cdot \nabla_{\boldsymbol{v}_s} f_s = 0, \tag{6}$$

$$-2\lambda^2 \Delta\phi = n_i - n_e,\ n_s = \int f_s dv_s, \tag{7}$$

and the normalized nonlinear Poisson equation (4) is,

$$-2\lambda^2 \Delta\phi = n_i - \exp\left(\frac{\phi - \phi_0}{T_e}\right),\ n_i = \int f_i dv_i. \tag{8}$$

Although the code allows arbitrary species, the single-charged ion (s = i) or electron (s = e) is considered in this paper. As a result, one can obtain $q_e = -1$, $q_i = 1$ from Eqs. (6). For direct kinetic method, the key is to obtain the distribution function f_s. Once the distribution function f_s is known, the conservative variables $\boldsymbol{W}_s$ for species s can be obtained by

$$\boldsymbol{W}_s = (n_s, n_s \boldsymbol{u}_s, E_{ks})^{\mathrm{T}} = \int \boldsymbol{\psi}_s f_s d\boldsymbol{v}_s, \tag{9}$$

where $\boldsymbol{\psi}_s = (1, \boldsymbol{v}_s, |\boldsymbol{v}_s|^2/2)^{\mathrm{T}}$ is the collision invariant, $\boldsymbol{u}_s$ is the macroscopic velocity and E_{ks} is the kinetic energy.

In the following section, we aim to propose a novel noiseless plasma kinetic solver for plasma-material interactions based on structured interface-independent meshes.

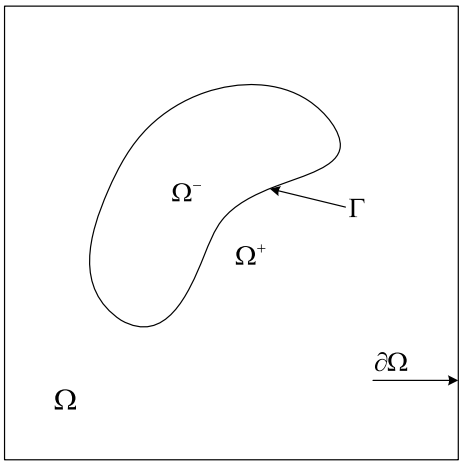

Fig. 1. A sketch of the domain for the interface problem.

3. Numerical methods

In this section, we will present a novel noiseless kinetic plasma solver, termed IFE-CSL, for the complex plasma surface interaction based on structured interface-independent meshes. The major steps of the proposed method include the IFE solver for field equation, the CSL and HWGC scheme for Vlasov equation, as well as the integration of two solvers.

In order to solve the multi-dimensional VP system, we firstly split Vlasov Eq. (1) as follows,

$$\partial_t f_s + \boldsymbol{v}_s \cdot \nabla_{\boldsymbol{x}} f_s = 0, \tag{10}$$

$$\partial_t f_s + \frac{q_s}{m_s} \boldsymbol{E} \cdot \nabla_{\boldsymbol{v}_s} f_s = 0. \tag{11}$$

It is well known that Eq. (1) can be achieved second order in time by solving Eq. (10) for a half time step, then solving Eq. (11) for a whole time step, followed by solving Eq. (10) for a second half time step, i.e., the Strang splitting. Specifically, the numerical update from $f_s^k(\boldsymbol{x}, \boldsymbol{v})$ (the solution at $t^k = k\Delta t$) to $f_s^{k+1}(\boldsymbol{x}, \boldsymbol{v})$ can be written in the form [46],

$$f_s^*(\boldsymbol{x}, \boldsymbol{v}) = f_s^k(\boldsymbol{x} - \boldsymbol{v}\Delta t/2, \boldsymbol{v}), \tag{12}$$

$$f_s^{**}(\boldsymbol{x}, \boldsymbol{v}) = f_s^*\left(\boldsymbol{x}, \boldsymbol{v} - \frac{q_s}{m_s}\boldsymbol{E}\Delta t\right), \tag{13}$$

$$f_s^{k+1}(\boldsymbol{x}, \boldsymbol{v}) = f_s^{**}(\boldsymbol{x} - \boldsymbol{v}\Delta t/2, \boldsymbol{v}). \tag{14}$$

It should be noted that Eqs. (12) and (14) represent the plasma transportation in physical space, while Eq. (13) represents the plasma acceleration in velocity space. It should be noted that the transportation coefficient in both Eqs. (12), (13), (14) are constant at each time step. As a result, Eqs. (12), (13), (14) can be further solved exactly by the single splitting operators in each dimension. Then the multi-dimensional Vlasov Eq. (1) is reduced to a succession of one-dimensional problem. This choice not only provides more alternative methods to solve the Eq. (1), but also makes the multi-dimensional simulation to be more practical [37]. Now, the key is to obtain the time evolution of the distribution function $f_s^{k+1}(\boldsymbol{x}, \boldsymbol{v})$ and the electrostatic field $\boldsymbol{E}$.

3.1. Immersed finite element method for the field equation

In this section, we present the immersed finite element (IFE) method [5] to solve the field equation to obtain the electrostatic field $\boldsymbol{E}$. The IFE method is the further extension of finite element (FE) method which utilizes the structured mesh independent of the interface to solve the partial differential equation with discontinuities in the coefficients. The IFE method includes interface elements whose interiors are cut through by the interface and non-interface elements that does not involve the interface. Standard FE basis functions are used for non-interface elements, while special basis functions satisfying interface jump conditions are implemented for interface elements. As a result, the only difference between IFE and traditional FE is the choice of different basis functions on the interface elements, which leads to a convenient implementation of the IFE method based on FE method. Below we describe the IFE method for the Poisson equation.

As shown in Fig. 1, we assume that $\Omega \subset R^2$ is a rectangular domain. The IFE method uses meshes that are independent of the interface and allows the interface to pass through the element. A smooth interface curve Γ separates Ω into subdomains Ω^- and Ω^+ such that $\Omega = \Omega^+ \cup \Omega^- \cup \Gamma$. Consider the following interface problem model:

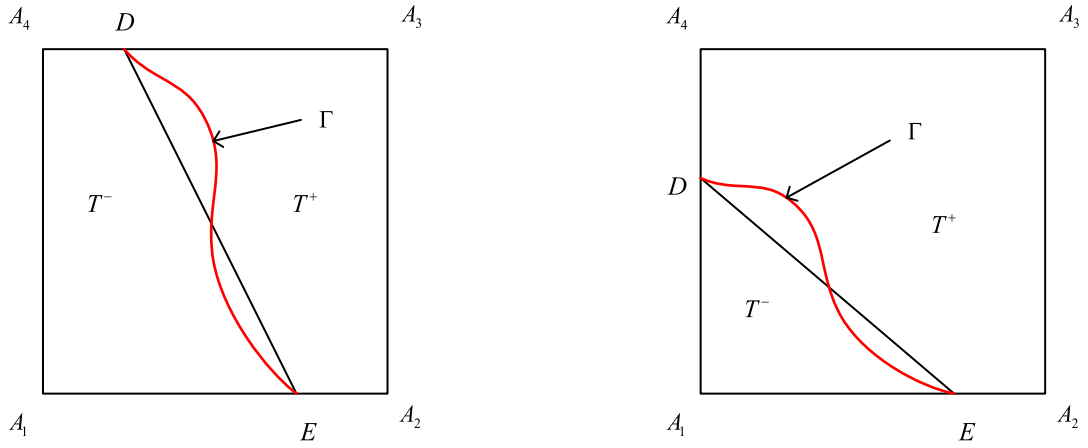

Fig. 2. Two typical interface elements.

$$-\nabla \cdot (\varepsilon \nabla \phi) = \rho, \tag{15}$$

where ρ is the charge density, and the material-dependent coefficient $\varepsilon(x, y)$ is a piecewise constant function defined by

$$\varepsilon(x, y) = \begin{cases} \varepsilon^-, (x, y) \in \Omega^-, \\ \varepsilon^+, (x, y) \in \Omega^+. \end{cases} \tag{16}$$

Here we assume that the solution on $\partial\Omega$ satisfies the Dirichlet and Neumann boundary conditions,

$$\phi|_{\partial\Omega_D} = g_D, \tag{17}$$

$$\varepsilon \frac{\partial \phi}{\partial \boldsymbol{n}}\bigg|_{\partial\Omega_N} = g_N, \tag{18}$$

where $\partial\Omega_D$ and $\partial\Omega_N$ are Dirichlet and Neumann boundary conditions such that $\partial\Omega = \partial\Omega_D \cup \partial\Omega_N$. Besides, the electric field is discontinuous across the interface Γ with the following jump conditions:

$$[\phi]|_\Gamma = 0, \tag{19}$$

$$\left[\varepsilon \frac{\partial \phi}{\partial \boldsymbol{n}}\right]\bigg|_\Gamma = 0, \tag{20}$$

where $[\phi]|_\Gamma = (\phi|_{\Omega^+})_\Gamma - (\phi|_{\Omega^-})_\Gamma$ is the jump of ϕ across Γ, and $\boldsymbol{n}$ is the unit normal vector of curve Γ pointing from Ω^- to Ω^+.

Let T_h be a family of rectangular meshes of the domain Ω. The sets of interface elements and non-interface elements are denoted by T_h^i and T_h^n. On the non-interface element $T \in T_h^n$, the local finite element space is spanned by the four standard bilinear nodal basis functions $\psi_i(x, y)(i = 1, 2, 3, 4)$. On the interface element $T \in T_h^i$, as shown in Fig. 2, with vertices $A_i(i = 1, 2, 3, 4)$ is intersected by curve Γ at two points denoted by D and E, and the line $\overline{DE}$ separates the element T into T^+ and T^-. Then four piecewise 2D linear immersed finite element basis functions can be introduced in [47],

$$\psi_i = \begin{cases} \psi_i^-(x, y) = a_i^- x + b_i^- y + c_i^- + d_i^- xy\ , (x, y) \in T^-, \\ \psi_i^+(x, y) = a_i^+ x + b_i^+ y + c_i^+ + d_i^+ xy\ , (x, y) \in T^+, \end{cases} (i = 1, 2, 3, 4). \tag{21}$$

To enclose Eq. (21), we consider the following constraints:

(1) Nodal value conditions

$$\psi_i(A_j) = \begin{cases} 1, \text{if } i = j, \\ 0, \text{if } i \neq j, \end{cases} (i, j = 1, 2, 3, 4); \tag{22}$$

(2) The continuity at points D, E and $\frac{D+E}{2}$

$$\begin{cases} \psi_i^+(D) = \psi_i^-(D), \\ \psi_i^+(E) = \psi_i^-(E), \\ \psi_i^+(\frac{D+E}{2}) = \psi_i^-(\frac{D+E}{2}), \end{cases} (i = 1, 2, 3, 4); \tag{23}$$

where $\frac{D+E}{2}$ is the middle point of the line $\overline{DE}$.

(3) Flux continuity on the line $\overline{DE}$

$$\int_{\overline{DE}} \left(\varepsilon^- \frac{\partial \psi_i^-}{\partial \boldsymbol{n}_{\overline{DE}}} - \varepsilon^+ \frac{\partial \psi_i^+}{\partial \boldsymbol{n}_{\overline{DE}}} \right) ds = 0, \ (i = 1, 2, 3, 4), \tag{24}$$

where $\boldsymbol{n}_{\overline{DE}}$ is the unit vector perpendicular to the line $\overline{DE}$ pointing from T^- to T^+. With Eqs. (22), (23), and (24), the IFE basis functions (21) can be uniquely determined. For simplicity of presentation, we omit the details.

For each element $T \in T_h$, we define

$$S_h(T) = \begin{cases} S_h^{non}(T), & \text{if } T \text{ is a non-interface element,} \\ S_h^{int}(T), & \text{if } T \text{ is an interface element.} \end{cases}$$

The local finite element space, $S_h(T)$, is defined in this study as either a regular (non-interface) space, denoted as $S_h^{non}(T)$, or an interface space, denoted as $S_h^{int}(T)$, depending on the characteristics of the element T.

Then let $N_h = \{X_i\}_{i=1}^N$ denote the set of nodes in T_h, where N is the total number of mesh nodes. Define $\psi_i(X)$ $(i = 1, ..., N)$ to be a piecewise bilinear function on Ω such that

$$\psi_i \big|_T \in S_h(T), \ \forall T \in T_h \text{ and } \psi_i(X_j) = \delta_{ij}, \ \forall X_j \in N_h.$$

Finally, the bilinear IFE space on the whole domain Ω becomes

$$S_h(\Omega) = span\{\psi_i(x), \ 1 \le i \le N\}.$$

Once the basis function is determined, we could apply the Galerkin method for solving the interface model (15). Let $H^1(\Omega)$ denote the regular Sobolev space and define $H_0^1(\Omega) = \{\psi : \psi \in H^1(\Omega), \psi = 0 \text{ on } \partial\Omega\}$. Besides, we use $(\cdot, \cdot)$ to denote L^2 inner product on domain Ω and $\langle \cdot, \cdot \rangle$ to denote L^2 inner product on the boundary $\partial\Omega$, e.g., $(\boldsymbol{u}, \boldsymbol{v}) = \int_\Omega \boldsymbol{u} \cdot \boldsymbol{v} d\Omega$ and $\langle \boldsymbol{u}, \boldsymbol{v} \rangle = \int_{\partial\Omega} \boldsymbol{u} \cdot \boldsymbol{v} ds$. Then the associated weak form of Eq. (15) can be written as the following system,

$$(\nabla\phi, \nabla\psi) = (\rho, \psi) + \langle \nabla\phi \cdot \boldsymbol{n}, \psi \rangle, \forall \psi \in H_0^1(\Omega). \tag{25}$$

Then we introduce finite dimensional subspace $\phi_h \subset H^1(\Omega)$ to discretize Eq. (25). Choosing the set of basis functions $\{\psi_j\}$ span above subspace, we can then approximate the electric potential by

$$\phi_h(x, y) = \sum_{j=1}^{N} \phi_j \psi_j(x, y). \tag{26}$$

Plugging Eq. (26) into Eq. (25), we can obtain

$$M\boldsymbol{\Phi} = \boldsymbol{b} + \boldsymbol{F}, \tag{27}$$

where the Poisson matrices M, source vector $\boldsymbol{b}$ and boundary vector $\boldsymbol{F}$ are defined as

$$\begin{cases} M = \left[\left(\psi_i, \psi_j \right) \right]_{i,j=1,...,N}, \\ \boldsymbol{b} = \left[(\rho, \psi_i) \right]_{i=1,...,N}, \\ \boldsymbol{F} = \left[\langle \nabla\phi \cdot \boldsymbol{n}, \psi_i \rangle \right]_{i=1,...,N}, \\ \boldsymbol{\Phi} = \left[\phi_j \right]_{j=1,...,N}. \end{cases} \tag{28}$$

It should be noted that the produce, e.g., assembling Poisson matrices M, source vector $\boldsymbol{b}$ and boundary vector $\boldsymbol{F}$, of IFE is same as that of FE, one can refer to [5,47] for more details. Since the information of object has been considered in the basis function (21) in IFE, we do not need to pay extra effort to handle the boundary condition for object interface Γ. To improve the efficiency of the IFE method, the Poisson matrices M in Eq. (27) is assembled with sparse storage technology. Then Eq. (27) becomes a sparse system, which is solved by GMRES iterative scheme [48] in this paper.

3.2. Conservative semi-Lagrangian scheme for the Vlasov equation

In this section, we present the conservative semi-Lagrangian scheme to solve the kinetic transportation equation Eqs. (12), (13), (14). Obviously, the Eqs. (12), (13) and (14) can be further written is a unified form,

$$\partial_t f_s + \partial_x (a f_s) = 0, \tag{29}$$

where a denotes as velocity $\boldsymbol{v}$ in Eqs. (12) and (14), or electrostatic force $\frac{q_s}{m_s}\boldsymbol{E}$ in Eq. (13). Obviously, Eq. (29) is the linear hyperbolic equation, which allows for the implementation of the conservative scheme following the characteristics lines.

Here we employ the CSL scheme, a revised positive flux-conservative (PFC) scheme [35,37], which is briefly reviewed as follows:

Firstly, we introduce a set of mesh points $\{x_{i+1/2}\}_{I_i}$ of the computational domain $[x_{\min}, x_{\max}]$, where $I_i = [x_{i-1/2}, x_{i+1/2}]$ are uniform numerical cells with centers $x_i = (x_{i-1/2} + x_{i+1/2})/2$ and cell sizes $\Delta x_i = x_{i+1/2} - x_{i-1/2}$. We use the $f_i^k = \frac{1}{\Delta x}\int_{x_{i-1/2}}^{x_{i+1/2}} f(x,t^k)dx$ to denote the cell averages of the solution over cell I_i. Tracking characteristic lines of the cell $[x_{i-1/2}, x_{i+1/2}]$ backward, we can find its upstream cell $[x_{i-1/2} - a\Delta t, x_{i+1/2} - a\Delta t]$, which is denoted as $[x^*_{i-1/2}, x^*_{i+1/2}]$. Accordingly, we have

$$\int_{x_{i-1/2}}^{x_{i+1/2}} f(x,t^{k+1})dx = \int_{x^*_{i-1/2}}^{x^*_{i+1/2}} f(x,t^k)dx\,,$$

which can be further rewritten in the flux form,

$$f_i^{k+1} = f_i^k + F_{i-1/2} - F_{i+1/2}\,, \tag{30}$$

where $F_{i-1/2} = \frac{1}{\Delta x}\int_{x_{i-1/2}-a\Delta t}^{x_{i-1/2}} f^k dx$ and $F_{i+1/2} = \frac{1}{\Delta x}\int_{x_{i+1/2}-a\Delta t}^{x_{i+1/2}} f^k dx$.

Then we present the flux $F_{i+1/2}$ in the third order scheme in the case of $\varphi < 1$ and $a > 0$ [35],

$$F_{i+1/2} = \left(f_i^k + \frac{1}{6}(2-|\varphi|)(1-|\varphi|)\left(f_{i+1}^k - f_i^k\right) + \frac{1}{6}(1-|\varphi|)(1+|\varphi|)\left(f_i^k - f_{i-1}^k\right)\right)\varphi\,, \tag{31}$$

where $\varphi = a\Delta t/\Delta x$ is related to CFL condition. Note that the case of $a \le 0$ is mirror symmetric with respect to x_i of the above procedure, and for $\varphi \ge 1$, it can be handled with a whole grid shift followed by the cases of $\varphi < 1$.

To achieve high-order accuracy, we adopt a general high-order parametrized positivity-preserving (PP) limiter in [38], which is designed as modifying the high order numerical flux towards the first order monotone flux in the following way

$$\hat{F}_{i+1/2} = \varepsilon_{i+1/2}\left(F_{i+1/2} - f_{i+1/2}\right) + f_{i+1/2}\,, \tag{32}$$

where $f_{i+1/2} = \varphi f_i^k$ is the first order flux, and $\varepsilon_{i+1/2} \in [0,1]$ is the positivity-preserving limiter to ensure the positivity of the function f_i^{k+1} in Eq. (30). We denote $d_{i\pm1/2} = F_{i\pm1/2} - f_{i\pm1/2}$ and $p_i = d_{i-1/2} - d_{i+1/2} - \delta_i^k$, the $\varepsilon_{i+1/2}$ can be given by the following formulas [37,38],

$$\varepsilon_i^l = \begin{cases} \min\left(1,\ \delta_i^k/d_{i-1/2}\right), & d_{i-1/2} < 0 \text{ and } \ d_{i+1/2} \le 0, \\ \delta_i^k/\left(d_{i-1/2} - d_{i+1/2}\right), & d_{i-1/2}d_{i+1/2} < 0 \text{ and } p_i < 0, \\ 1, & \text{else}, \end{cases}$$

$$\varepsilon_i^r = \begin{cases} \min\left(1, -\delta_i^k/d_{i+1/2}\right), & d_{i-1/2} \ge 0 \text{ and } \ d_{i+1/2} > 0, \\ \delta_i^k/\left(d_{i-1/2} - d_{i+1/2}\right), & d_{i-1/2}d_{i+1/2} < 0 \text{ and } p_i < 0, \\ 1, & \text{else}, \end{cases}$$

where $\varepsilon_{i+1/2} = \min\left(\varepsilon_i^r, \varepsilon_{i+1}^l\right)$.

Finally, we employ the modified flux $\hat{F}_{i\pm1/2}$ to replace the flux $F_{i\pm1/2}$ in Eq. (30) to evolve the function f_i^{k+1},

$$f_i^{k+1} = f_i^k + \hat{F}_{i-1/2} - \hat{F}_{i+1/2}\,. \tag{33}$$

The using of third PFC scheme [35] and the general high order PP limiter [38] make the current CSL scheme exactly preserve mass and positivity of the distribution function with third spatial accuracy [37], when periodic boundary conditions are applied.

To conveniently and efficiently describe the evolution of particles dynamic around the plasma-material interface, we apply the half-way ghost-cell (HWGC) method [44] to CSL within the Cartesian mesh. As shown in Fig. 3, we divide all Cartesian cells in the computational area into three types: solid cells, fluid cells and ghost cells. Among them, the solid and the fluid cell denote the solid material and plasma, respectively. The solid cell has at least one link intersected by the interface is further transformed to be the ghost cell, which denotes plasma-material interactions. For the sake of simplicity, the physical interactions are approximated by the middle of the mesh between the ghost and fluid cells.

Taking ghost cell center G in Fig. 3 for example, one needs the distribution function $f_s(x_{I_n}, \boldsymbol{v}, t)$ at intersection nodes (I_1, I_2) to obtain the distribution function $f_s(x_G, \boldsymbol{v}, t)$ at G. The information of outflow at intersection nodes (I_1, I_2) can be extrapolated from the neighboring fluid cells,

$$f_s(x_{I_n}, \boldsymbol{v}, t) = 1.5 f_s(x_{F_{n,1}}, \boldsymbol{v}, t) - 0.5 f_s(x_{F_{n,2}}, \boldsymbol{v}, t),\ \ \boldsymbol{v}\cdot\boldsymbol{n} < 0, \tag{34}$$

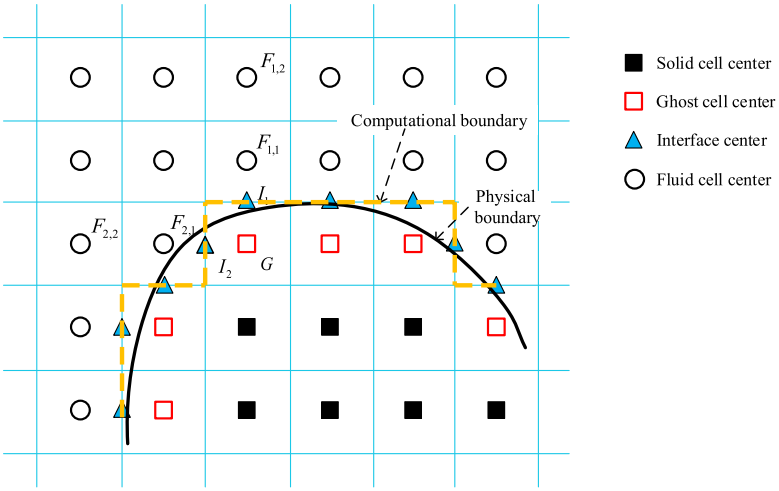

Fig. 3. Schematic of the HWGC method. Point G is the center of a ghost cell. I_1 and I_2 are artificially reset at the middle of the mesh. $F_{1,1}$ and $F_{2,1}$ are the neighboring fluid cell centers, which is in mirror symmetry with G regarding to the computational boundary. $F_{1,2}$ and $F_{2,2}$ are two further fluid cell centers along the grids. The black solid lines and yellow dot lines between the ghost and fluid cell center are physical boundary and computational boundary, respectively.

where $\boldsymbol{n}$ is the normal vector of the physical boundary. As for the inflow at intersections, the zero-inflow boundary conditions are employed in this paper,

$$f_s(x_{I_n}, \boldsymbol{v}, t) = 0, \ \boldsymbol{v} \cdot \boldsymbol{n} > 0. \tag{35}$$

Equation (35) is reasonable because the object (a conductor) completely absorbs the particles, resulting in no reflection of particles back into the system.

Then, the distribution functions at the ghost G can be obtained by extrapolation from points I_n and $F_{n,1}$ as

$$f_s(x_G, \boldsymbol{v}, t) = \frac{1}{N_g} \sum_{n=1}^{N_g} [2 f_s(x_{I_n}, \boldsymbol{v}, t) - f_s(x_{F_{n,1}}, \boldsymbol{v}, t)], \tag{36}$$

where N_g is total intersections around ghost G.

3.3. Integration of IFE and CSL

In this section, we will introduce how to integrate the IFE and CSL methods into a unified system. The CSL scheme provides the charge density ρ to the IFE method to form the right hand side vector $\boldsymbol{b}$ of the linear or nonlinear system Eq. (27) in IFE, while the IFE method accurately solving the interface problems on Cartesian meshes provides the electrostatic field $\boldsymbol{E}$ in Eq. (13) for CSL to accelerate the plasma. It should be noted that the object information is critical to both IFE and CSL because the intersection points between the mesh lines and object surfaces are the key to define the IFE basis functions (see Section 3.1) and the plasma hitting an object need to be appropriately handled in CSL (see HWGC method in Section 3.2).

On the one hand, in order for using the IFE method to solve the interface Poisson's equation (15) for the electrostatic potential ϕ, the electric charge density ρ in Eq. (15) needs to be provided by the CSL scheme. For the full kinetic model, i.e., both ion and electron dynamics are described by the CSL scheme, Eq. (15) is just the linear equation (2). Then we can obtain the charge density ρ by taking the moment of distribution function,

$$\rho = \int q f_i d\boldsymbol{v}_i - \int q f_e d\boldsymbol{v}_e. \tag{37}$$

Obviously, now Eq. (27) is a linear system, which can be directly solved by the GMRES algorithm. However, for the hybrid kinetic model, i.e., the Boltzmann approximation Eq. (3) is used for describing electron dynamic, Eq. (15) becomes the nonlinear equation (4). Then the charge density ρ is obtained by

$$\rho = \int q f_i d\boldsymbol{v}_i - q n_0 \exp\left(\frac{q(\phi - \phi_0)}{k_B T_e}\right). \tag{38}$$

The electric potential ϕ on the right hand side of Eq. (38) makes Eq. (27) become a nonlinear system, which can be written in the following form,

$$M\boldsymbol{\Phi} = \boldsymbol{b}_0 + \boldsymbol{b}_x(\boldsymbol{\Phi}) + \boldsymbol{F}, \tag{39}$$

where $\boldsymbol{b} = \boldsymbol{b}_0 + \boldsymbol{b}_x(\boldsymbol{\Phi})$, $\boldsymbol{b}_0 = \left[\left(\int q f_i d\boldsymbol{v}_i, \psi_i\right)\right]_{i=1,\dots,N}$, and $\boldsymbol{b}_x = \left[\left(-qn_0 \exp\left(\frac{q(\phi-\phi_0)}{k_B T_e}\right), \psi_i\right)\right]_{i=1,\dots,N}$. In current paper, we use Newton's method to solve the nonlinear system (39),

$$\begin{cases} \boldsymbol{\Phi}^{k+1} = \boldsymbol{\Phi}^k - J^{-1}\boldsymbol{R}(\boldsymbol{\Phi}^k), \\ \boldsymbol{R}(\boldsymbol{\Phi}) = M\boldsymbol{\Phi} - (\boldsymbol{b}_0 + \boldsymbol{b}_x(\boldsymbol{\Phi})), \end{cases} \tag{40}$$

where $J = \frac{\partial \boldsymbol{R}}{\partial \boldsymbol{\Phi}}$ is the Jacobian matrix. In the practical computation, we firstly solve the system $J\boldsymbol{y} = \boldsymbol{R}(\boldsymbol{\Phi})$ in the k-th iteration step, then update the solution as $\boldsymbol{\Phi}^{k+1} = \boldsymbol{\Phi}^k - \boldsymbol{y}$. The iteration for solving Eq. (40) is ceaselessly repeated unless the L^2 norm of $\boldsymbol{y}$ is smaller than 10^{-8}.

On the other hand, the IFE solution of the electrostatic potential ϕ is utilized to compute the electric field $\boldsymbol{E}$ which needs to be evaluated at each cell center in CSL for accelerating plasma. The electric field $\boldsymbol{E}$ can be easily obtained from the electric potential ϕ by

$$\boldsymbol{E}(x, y) = -\nabla\phi(x, y). \tag{41}$$

To more accurately obtain the electric field at the interface, thanks to the basis function used in the IFE methods, we could apply the following equation to approximate the electric potential at point (x, y) in an element T,

$$\phi_T(x, y) = \sum_{i=1}^{4} \phi_i \psi_{i,T}(x, y), \tag{42}$$

where ϕ_i are the IFE solution of the potential at the four vertices of element T, while $\psi_{i,T}$ are the local IFE basis functions. Plugging Eq. (42) into Eq. (41), we can obtain the electric field as follows,

$$\boldsymbol{E}_x(x, y) = -\sum_{i=1}^{4} \phi_i \frac{\partial \psi_{i,T}(x, y)}{\partial x}, \quad \boldsymbol{E}_y(x, y) = -\sum_{i=1}^{4} \phi_i \frac{\partial \psi_{i,T}(x, y)}{\partial y}. \tag{43}$$

It should be noted that Eq. (43) is equivalent to the traditional Finite Difference (FD) discretization of Eq. (41) in the non-interface element. However, Eq. (43) is more accurate than FD discretization in the interface element where the internal and external potential of objects are discontinuous [10].

Finally, we explain how the numerical time step is determined for the proposed IFE-CSL. In the traditional explicit Eulerian scheme, the numerical time step is subject to the Courant-Friedrichs-Lewy (CFL) restriction and is calculated as $\Delta t = \min(\Delta t_x, \Delta t_v)$. Here $\Delta t_x = C\Delta \boldsymbol{x}_{\min}/|\boldsymbol{v}|_{\max}$, and $\Delta t_v = C\Delta \boldsymbol{v}_{\min}/|\boldsymbol{E}|_{\max}$ are the time steps associated with the transportation velocity $\boldsymbol{v}$ in Eq. (10) and the electrostatic field $\boldsymbol{E}$ in Eq. (11). The parameters $0 < C < 1$, $|\boldsymbol{v}|_{\max}$, and $|\boldsymbol{E}|_{\max}$ represent the CFL number, maximum transportation velocity, and maximum electrostatic field, respectively. Additionally, $\Delta \boldsymbol{x}_{\min}$ and $\Delta \boldsymbol{v}_{\min}$ denote the minimum physical grid spacing and velocity grid spacing, respectively.

Thanks to the use of CSL, the numerical time step in proposed IFE-CSL is not limited by the CFL restriction mentioned above. However, to simplify the implementation of the general boundary conditions in the physics space [Eq. (10)], we use the time step $\Delta t = \Delta t_x$ in all kinetic simulations, ensuring that particles do not travel more than one grid cell during the interactions of plasma and material. Note homogeneous Dirichlet or periodic boundary conditions generally used in the velocity space [Eq. (11)] allow for easy handling in CSL. Therefore, IFE-CSL still preserves the advantages of CSL, as Δt is not restricted by Δt_v. This is particularly beneficial in plasma simulations involving large electric forces or fine grids in the velocity space [33].

3.4. Algorithm

To provide a clearer understanding of the proposed IFE-CSL, here we present its evolution procedure. Starting from initial distribution function f_s^k and specific input geometric information, the evolution procedure of proposed method from t^k to t^{k+1} can be described as follows:

(1) Calculate function f_s^* from f_s^k by solving Eq. (12) with Lie Splitting in physical space for $\Delta t/2$.
  (a) Compute the third order physical flux according to Eq. (31) in each physical direction;
  (b) Correct the physical flux with parametrized PP limiter by Eq. (32) in each physical direction;
  (c) Obtain function f_s^* Eq. (33) in each physical direction.
(2) Calculate charge density ρ by solving Eq. (37) for linear system (2) or Eq. (38) for nonlinear system (4).
(3) Compute electric potential ϕ by solving Eq. (27) for linear system (2) or Eq. (39) for nonlinear system (4).
(4) Calculate the electric field $\boldsymbol{E}$ according to Eq. (43).
(5) Update f_s^{**} by solving Eq. (13) with Lie Splitting in velocity space for Δt.
(6) Update f_s^{k+1} by solving Eq. (14) with Lie Splitting in physical space for $\Delta t/2$.

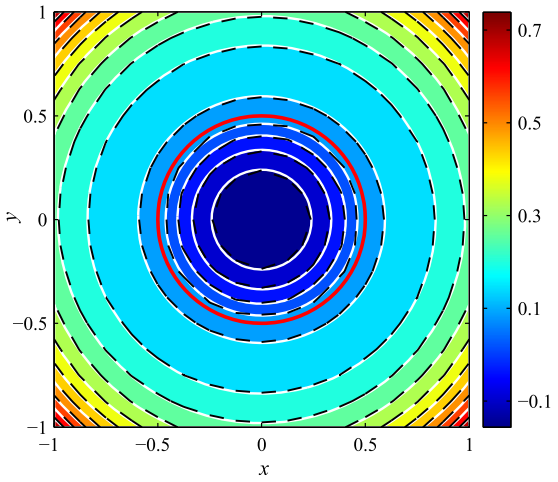

Fig. 4. The contour of electric potential with $N_x = 128$, where the black dashed lines and the white solid lines denote the theoretical and numerical results, respectively. The red circular curve represents the interface.

It should be noted that the process of step (5) and (6) in each dimension is similar to that of step (1), which are omitted for simplicity of presentation. Besides, in each iteration of whole system, the process of step (2) and (3) for nonlinear system (4) is ceaselessly repeated unless the criterion of Newton iteration is satisfied.

4. Numerical experiments

In this section, four numerical experiments, including the elliptic interface problem, classical plasma sheath, the sheath with rough wall, and plasma past a charged cylinder are implemented to validate the proposed IFE-CSL. The first one is two-dimensional in physical space, while the others are two-dimensional in both physical space and velocity space. Fully kinetic simulation governed by Eqs. (1) and (2) is implemented in the two plasma sheath problems, while the hybrid kinetic simulation governed by Eqs. (1) and (4) is used in the last numerical experiment.

4.1. Elliptic interface problem

In this section, a two-dimensional elliptic interface problem with homogeneous jump conditions is presented to validate the accuracy of the IFE method. More specifically, we assume that the computational domain is a rectangular area $\Omega = [-1, 1] \times [-1, 1]$, where a circular interface is located in the center. Then, the analytic solution of the potential can be constructed as [10]:

$$\begin{cases} \phi^-(x, y) = \frac{1}{\varepsilon^-} e^{x^2+y^2} + (\frac{1}{\varepsilon^+} - \frac{1}{\varepsilon^-}) e^{r_0^2}, & \text{if } r \le r_0, \\ \phi^+(x, y) = \frac{1}{\varepsilon^+} e^{x^2+y^2}, & \text{if } r > r_0, \end{cases}$$

where $r_0 = \pi/6.28$ is the radius of the circle, $\varepsilon^- = 1$, $\varepsilon^+ = 10$, and $r = \sqrt{x^2 + y^2}$. The electric charge density ρ can be obtained from Eq. (15),

$$\rho(x, y) = -4(1 + x^2 + y^2) e^{x^2+y^2}.$$

Besides, in all the four boundaries on $\partial\Omega$ the Dirichlet boundary conditions are implemented,

$$g_D(x, y) = \frac{1}{\varepsilon^+} e^{x^2+y^2}.$$

In our simulation, a moderate physical grid $N_x = N_y = 128$ is used to demonstrate the good performance of the IFE method on handling the interface problem. Fig. 4 shows the contour of the electric potential ϕ predicted by the IFE, together with the analytic solution ϕ_a; the numerical result predicted by IFE agrees well with the analytic solution even though the moderate physical grid is used. Then we test the spatial accuracy of the IFE. Table 1 shows the L^2 and H^1 errors and convergence order of IFE with different physical grids N_x. Clearly, the results show that the L^2 norm error has a second-order convergence rate, and the H^1 norm error has a first-order convergence rate, which are consistent with the expected optimal convergence rate of IFE.

The above arguments indicate that the IFE has higher accuracy and better convergence order in solving the elliptic interface problem. In addition, all the simulations presented in this section utilize sparse matrix storage, which makes the proposed IFE more practical in multidimensional simulations.

Table 1
L^2 and H^1 errors and convergence orders of IFE for the elliptic interface problem.

N_x	$\|\phi-\phi_a\|_0$	Order	$\|\phi-\phi_a\|_1$	Order
32	2.2623E-3	1.9957	9.1382E-2	0.9732
64	5.3492E-4	2.0804	4.5393E-2	1.0094
128	1.2608E-4	2.0849	2.3029E-2	0.9790
256	3.3454E-5	1.9141	1.2685E-2	0.8603

4.2. Plasma sheath

Now the IFE-CSL is applied to study the direct current sheath at a plasma-wall transition with the straight smooth wall, where an analytical solution can be obtained. Specifically, the classical direct current sheath of a material with floating potential is investigated.

In the domain $[0, L_x] \times [0, L_y]$, the sheath edge is set to be at $y = L_y$ and the wall is at $y = 0$, while the edge $x = 0$ and $x = L_x$ are periodic. Here we set the potential at the sheath edge to be zero, and consider the positive sheath $\phi(x, y) < \phi(x, y = L_y) = 0$ for $T_e \gg T_i$. The initial velocity distribution function (VDF) of electron follows,

$$f_e(x, y, v_x, v_y) = \begin{cases} \frac{n_{in} m_e}{2\pi k_B T_e} \exp\left(-\frac{m_e(v_x^2+v_y^2)}{2k_B T_e} + \frac{q\phi}{k_B T_e}\right), & v_y \le v_{ce}, \\ 0, & v_y > v_{ce}, \end{cases} \tag{44}$$

where $v_{ce} = \sqrt{2q(\phi - \phi_w)/m_e}$ is the cutoff velocity of the truncated electrons due to the potential drop in the sheath at y direction, n_{in} is the inject density number and ϕ_w is the wall potential at $y = 0$. The VDF of ion follows,

$$f_i(x, y, v_x, v_y) = \begin{cases} \frac{n_{in} m_i}{2\pi k_B T_i} \exp\left(-\frac{m_i}{2k_B T_i}\left(\sqrt{v_y^2 + \frac{2q\phi}{m_i}} - u_0\right)^2 - \frac{m_i v_x^2}{2k_B T_i}\right), & v_y \le v_{ci}, \\ 0, & v_y > v_{ci}, \end{cases} \tag{45}$$

where $v_{ci} = -\sqrt{2q|\phi|/m_i}$, and $u_0 = \sqrt{k_B T_e/m_i}$ is the Bohm velocity.

For $|q\phi_w|/k_B T_e \gg 1$, taking the zero moment of the Eq. (44), the electron density can be described as,

$$n_e = n_{in} \exp\left(\frac{q\phi}{k_B T_e}\right). \tag{46}$$

For the ion density with very low temperature, considering the law of energy conservation [33], the ion density can be approximated by,

$$n_i = n_{in}\left(1 + \frac{2q\phi}{m_i u_0^2}\right)^{-\frac{1}{2}}. \tag{47}$$

Obviously, the quasi-neutral assumption ($n_e = n_i$) holds true at the sheath edge $y = L_y$. Besides, consider the flux balance ($n_{iw}u_{iw} = n_{ew}u_{ew}$), where n_{iw} and u_{iw} as well as n_{ew} and u_{ew} are the number density and macro velocity for ions and electrons at $y = L_y$, then the expected wall potential ϕ_w should be,

$$\phi_w = -\frac{k_B T_e}{q} \ln\sqrt{\frac{m_i}{2\pi m_e}}. \tag{48}$$

Similar with other kinetic simulations for plasma sheath [49,50], the inject number density is set to be $n_{in} = 10^{14}$ m^{-3}, and the electron temperature is $T_e = 1$ ev. The sheath width is set to be $L_x = L_y = 20\lambda$, where λ is the electron Debye length. The ions with temperature $T_i = T_e/T_r$ are assumed to be hydrogen molecule, i.e., $m_i = 2m_r m_e$, where $m_r = 1836$ and $T_r = 10$ are mass ratio and temperature of the proton and electron respectively. Initially, electrons and ions follow the Eq. (44) and Eq. (45) with $\phi(x, y) = 0$ in the whole domain. The periodic boundary conditions are imposed on $x = 0$ and $x = L_x$ for both kinetic equation and field equation. Besides, the inject boundary, i.e., Eq. (44) for electron and Eq. (45) for ion, and zero-inflow boundary condition [33,51] are imposed on $y = L_y$ and $y = 0$ for kinetic equation, respectively, while the Dirichlet boundary [$\phi(x, y = Ly) = 0$] and Neumann boundary [$\partial\phi(x, y = 0)/\partial y) = -E_w$] are imposed on $y = L_y$ and $y = 0$ for field equation, respectively. Here E_w is the electric field at the wall, which can be determined by the charge accumulated by the ion and electron flux, i.e., $E_w = \frac{q}{\varepsilon}\int_{t'=0}^{t'=t} n_{iw}u_{iw} - n_{ew}u_{ew}dt'$.

In our simulation, the reference length, mass, density and temperature are set to be $x_0 = L_x$, $m_0 = m_i$, $n_0 = n_{in}$, $T_0 = T_i$, respectively. The discrete velocity space is set to be $[-4v_r, 4v_r] \times [-5v_r, 5v_r]$ for electrons and $[-4, 4] \times [-8, 1]$ for ions, where $v_r = \sqrt{2m_r T_r}$ is the thermal velocity ratio of electrons and ions. The whole phase space is discretized with $N = N_x \times N_y \times N_{vx} \times N_{vy}$, where the electrons and ions share the same physic grids with $N_x \times N_y = 10 \times 125$, the same

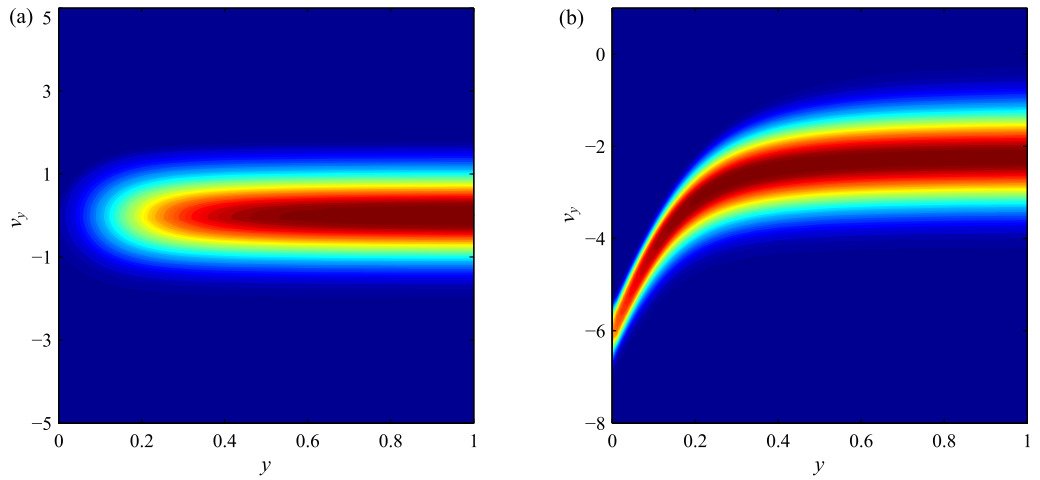

Fig. 5. Plasma sheath, phase-space plot of distribution function f of the electron (a) and the ion (b).

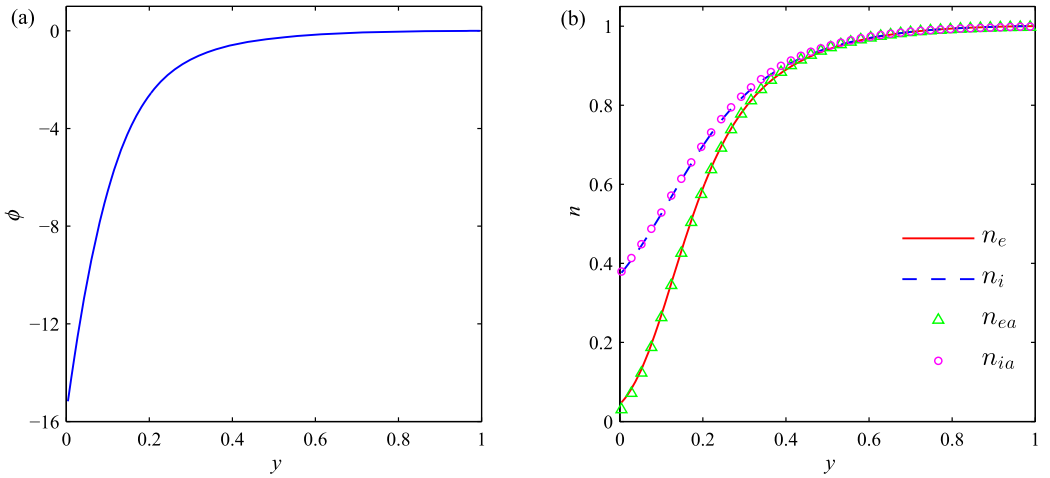

Fig. 6. Plasma sheath, electric potential ϕ (a) and number density n (b) at $x = L_x/2$ against physics space y. Note n_e and n_i are numerical electron and ion number density predicted by IFE-CSL, while n_{ea} and n_{ia} are theoretical solutions provided by Eq. (46) and Eq. (47).

velocity grids with $N_{vx} \times N_{vy} = 30 \times 110$, and the same time step with CFL number $C = 0.95$. Here we run this problem up to $t = 0.6$, i.e., $w_{pi}t = 12$, where w_{pi} is the ion plasma frequency.

Fig. 5 shows the phase space plot of the VDF of electrons and ions. Given the periodic boundary conditions are imposed on the x direction, only VDF at $x = L_x/2$ and $v_x = 0$ are presented for brevity. The warm electrons drop in the sheath due to the escape of fast electrons to the wall, while the cold ions become narrower due to the acceleration of the electric field. As shown in Fig. 5 (a), the VDF of electrons drops fast near the wall. Besides, the truncation of the VDF due to the potential barrier also can be seen. Although the truncation is slight, the velocity of electrons increases significantly due to fast thermal velocity. The acceleration of ions can be clearly seen in Fig. 5 (b), e.g., the velocity at sheath edge $y = L_y$ is -2.23, while the velocity at wall $y = 0$ is -6.08.

Fig. 6 shows the electric potential ϕ and number density n for plasma sheath. The steady electric potential can be clearly seen in Fig. 6 (a). Given the similar structure in the x direction, here we only present the electric potential at $x = L_x/2$ against the physic space y. Encouragingly, the numerical potential at the wall predicted by IFE-CSL agrees well with the theoretical prediction in Eq. (48) normalized by $\phi_0 = 2k_B T_i/q$. Besides, as shown in Fig. 6 (b), the numerical number density predicted by IFE-CSL are consistent with the theoretical solutions.

The above arguments indicate the IFE-CSL presents reliable solutions for plasma sheath. It should be noted that all results in this section are not time-averaged, in contrast to the PIC method which averages results to reduce noise, which can be seen as the present IFE-CSL is free from statistical noise.

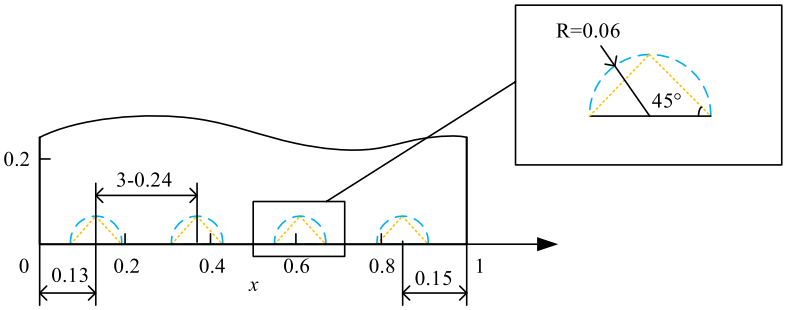

Fig. 7. Schematic of the computational domain for plasma sheath with rough wall.

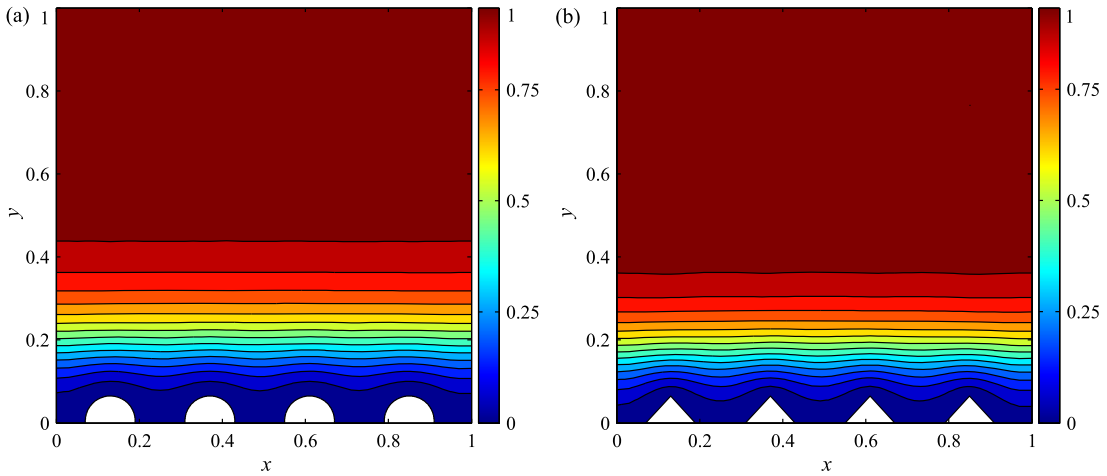

Fig. 8. Plasma sheath with rough wall, contours of the electron density for half-circle wave (a) and triangular wave (b).

4.3. Plasma sheath with rough wall

The previous section presents the classical plasma sheath on the smooth wall. However, the wall shapes might be complex geometry in the plasma engineering. In this section, the plasma sheath with two different wall shapes is presented to investigate the performance of IFE-CSL for plasma-material interactions on the complex interface, where both ion and electron dynamics are considered.

The simulation settings, in terms of the geometry, plasma parameters, initial and boundary condition, and reference system, in this section are same as that of section 4.2 unless otherwise stated, except the geometry of sheath wall. The wall shapes include triangular wave and half-circle wave, which mimic the periodic imperfections created by anomalous erosion [52]. Fig. 7 shows the size of the two different walls, which has been normalized by reference length L_x. On the wall, the Dirichlet boundary, $\phi = -20\phi_0$, is imposed for field equation, while the zero-inflow condition is imposed for kinetic equation.

In our simulation, the discrete velocity space is set to be $[-4v_r, 4v_r] \times [-5v_r, 5v_r]$ for electrons and $[-4, 4] \times [-8, 1]$ for ions, where $v_r = \sqrt{2m_r T_r}$ is the thermal velocity ratio of electrons and ions, $m_r = 1836$ and $T_r = 10$. The whole phase space for both ions and electrons is discretized with $N = N_x \times N_y \times N_{vx} \times N_{vy}$, where $N_x \times N_y = 50 \times 100$ and $N_{vx} \times N_{vy} = 50 \times 50$. The CFL number is set to be $C = 0.95$.

Fig. 8 shows the contours of the electron number density for two different walls. The similar behavior for the half-circle wave and triangle wave can be observed: a reduced electron number density with the periodical structure is formed around the wall, while the electron number density almost the same as those of the inject boundary exists in the main domain (from $y = 0.4$ to $y = 1$).

However, there are still slight deviations between the two waves, which can be more clearly seen in the charge density shown in Fig. 9. The different sheath structure for two walls can be clearly seen in the non-neutral regime (from $y = 0$ to $y = 0.3$). Besides, the charge density of the triangle wave is higher than that of the half-curve wave, especially at the interactions of the wall and plasma flow. It also can be seen that the width of the sheath in the half-curve is slight wider than that of the triangle wave.

To more clearly show the performance of the proposed IFE-CSL, in Fig. 10 we present the contours of the electric potential for the two walls. The continuous electric potential is obtained in the whole domain for the two cases, even in

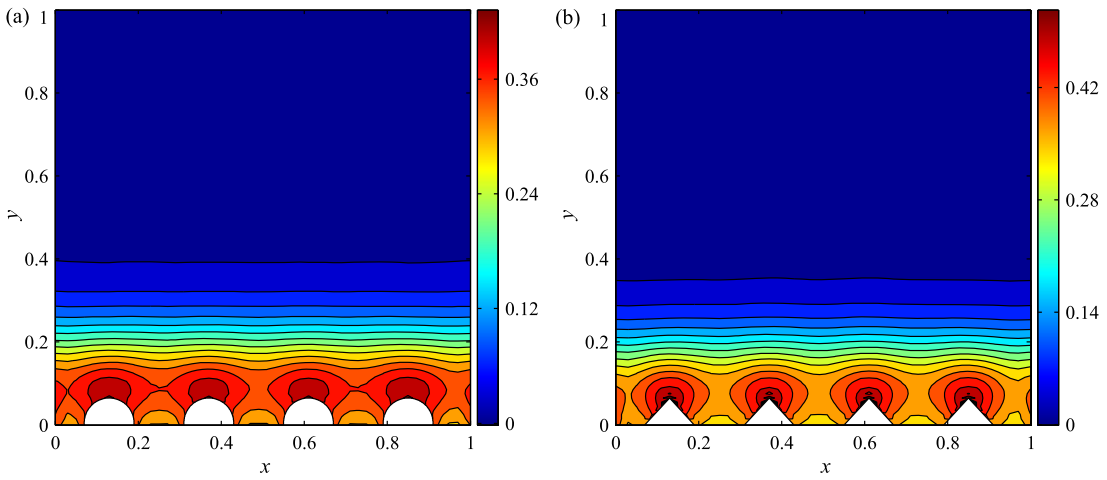

Fig. 9. Plasma sheath with rough wall, contours of the charge density for half-circle wave (a) and triangular wave (b).

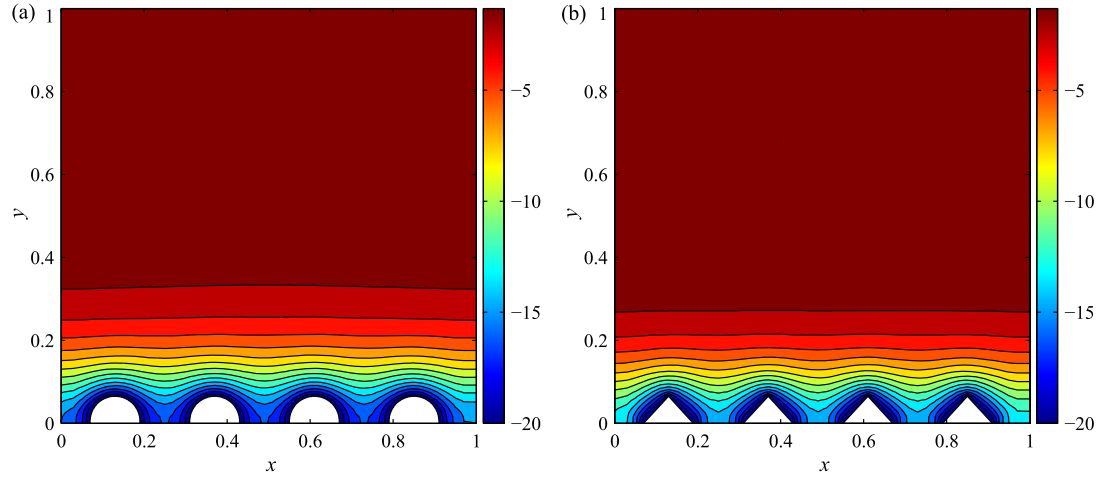

Fig. 10. Plasma sheath with rough wall, contours of the electric potential for half-circle wave (a) and triangular wave (b).

the surface of the plasma-material interaction. Especially, the interfaces of the numerical electric potential between plasma and the wall are consistent with expected interactions.

The above arguments indicate proposed IFE-CSL accurately predicts the interaction between ions, electrons dynamics and complex walls. The use of HWGC for plasma hitting the object and the IFE method for the linear Poisson equation makes the proposed IFE-CSL to be accurate for the complex plasma-material interaction even with moderately structured interface-independent meshes.

4.4. Plasma past a charged cylinder

In some applications, i.e., solar wind [53] and plasma expansion [20], one mainly focuses on the physics driven by the ion dynamics, a common approach has been to consider the electrons as an equilibrium massless fluid. This simplification leads to significant savings in computational time. In this section, plasma past a charged cylinder, which could represent a miniature Langmuir probe or a solar sail interacting with solar wind, is presented to investigate the performance of IFE-CSL for plasma-material interactions. Here the electrons follow the Boltzmann relationship and thus the nonlinear Poisson equation (4) is utilized. Besides, the IFE-PIC results are chosen as benchmark solutions.

Initially, there are no ions in the domain $[0, L_x] \times [0, L_y]$, where $L_x = 0.4$ m and $L_y = 0.2$ m. As shown in Fig. 11, a circle object with potential $\phi_w = -20$ V is immersed in the domain, where the circle center is $(x, y) = (0.375, 0)L_x$ and the radius is $R = 0.125L_x$. Note here half of the total system is simulated to reduce the computational time. Thus, the symmetry condition is imposed on $y = 0$. Ions are assumed to be hydrogen molecule and enter the domain at $x = 0$ with Maxwellian distribution, where the ions number density $n_{\text{in}} = 10^{10}$ m^{-3}, temperature $T_{\text{in}} = 0.15$ ev and the drift velocity $u_{x,\text{in}} = 7000$ m/s. As for the kinetic equation, the reflective boundary conditions are imposed on $y = 0$ and $y = L_y$, while the zero-inflow boundary condition is imposed on $x = L_x$. As for the field equation, the Dirichlet boundary $\phi = 0$ is applied

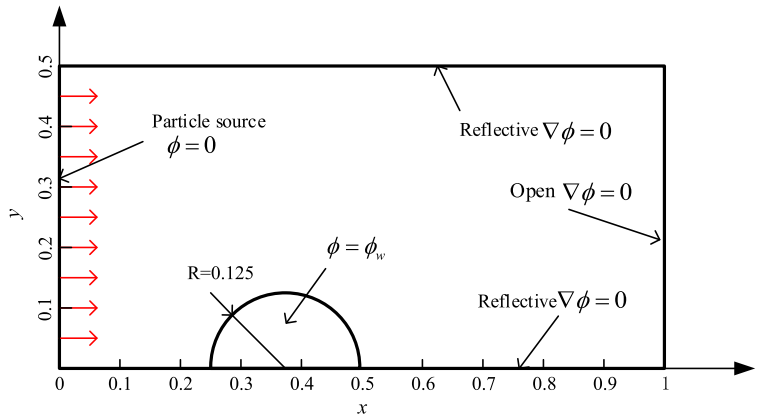

Fig. 11. Schematic of the computational domain normalized by L_x and boundary conditions.

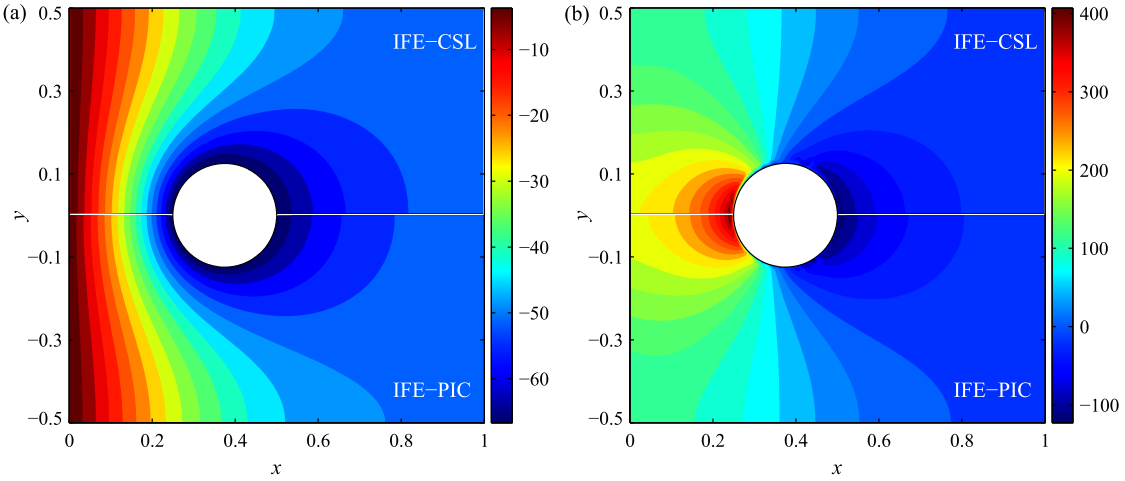

Fig. 12. Contours of the electrostatic potential (a) and the electric field E_x (b).

to $x = 0$, while the zero Neumann boundary $\nabla\phi = 0$ is applied to both $x = L_x$, $y = 0$ and $y = L_y$. Besides, the reference number density and temperature for electrons with Boltzmann approximation are 10^{10} m^{-3} and 1.5 ev.

In our simulation, the reference length, mass, density and temperature are set to be $x_0 = L_x$, $m_0 = m_i$, $n_0 = n_{in}$, $T_0 = T_{\text{in}}$, respectively. The whole phase space is discretized with $N = N_x \times N_y \times N_{vx} \times N_{vy}$, where the physic grids $N_x \times N_y = 160 \times 50$ and the velocity grids $N_{vx} \times N_{vy} = 120 \times 50$. The velocity space is set to be $[-5, 15] \times [-7, 7]$. Besides, the CFL number is set to be $C = 0.5$. Here we run this problem up to $t = 0.6$, i.e., $w_{pi}t = 12$.

Fig. 12 shows the contours of the electric potential ϕ and electric field E_x predicted by IFE-PIC (bottom) and proposed IFE-CSL (top) respectively. Here the object is modeled as a conductor held at a fixed potential by some virtual power supply. Note the conductor is included in the IFE-CSL with a high permittivity. As shown in Fig. 12 (a), a lens configuration, which is expected to focus ions into a region beyond the object, is formed around the object. Clearly, the electric potential and electric field predicted by IFE-CSL agrees well with IFE-PIC solution.

The more consistent details can be seen in Fig. 13, where the profiles of electric potential ϕ and field E_x at $y = 0$ and $y = 0.5$ are presented. As shown in Fig. 13 (a), at $y = 0$, the potential almost linearly decreases from 0 to ϕ_w in front of the object, while slightly increases behind the object. The sharp transition of the potential leads to the strong electric field E_x at $x = 0.25$ and $x = 0.5$ shown in Fig. 13 (b), while the potential and electric field at $y = 0.5$ decrease moderately. Encouragingly, the profiles of electric potential and field predicted by IFE-CSL also agree well with IFE-PIC solution.

However, there are still several disparities between IFE-PIC and current IFE-CSL, which can be seen in the ion number density in Fig. 14. When the ion stream flows around the negatively charged object which acts as a particle sink, the well-known ion focusing effect, plasma wake, forms behind the object. As shown in the figure, a high density region forms downstream the object because of the lensing effect seen in Fig. 12 (a). The inherent noise of IFE-PIC, especially in the low density region, is clearly apparent due to random process and particle effect, while the proposed IFE-CSL as a deterministic method is free from the noise. Although the numerical noise in IFE-PIC can be reduced by averaging the results over a large number of time steps, this strategy is ideally suited to steady flow.

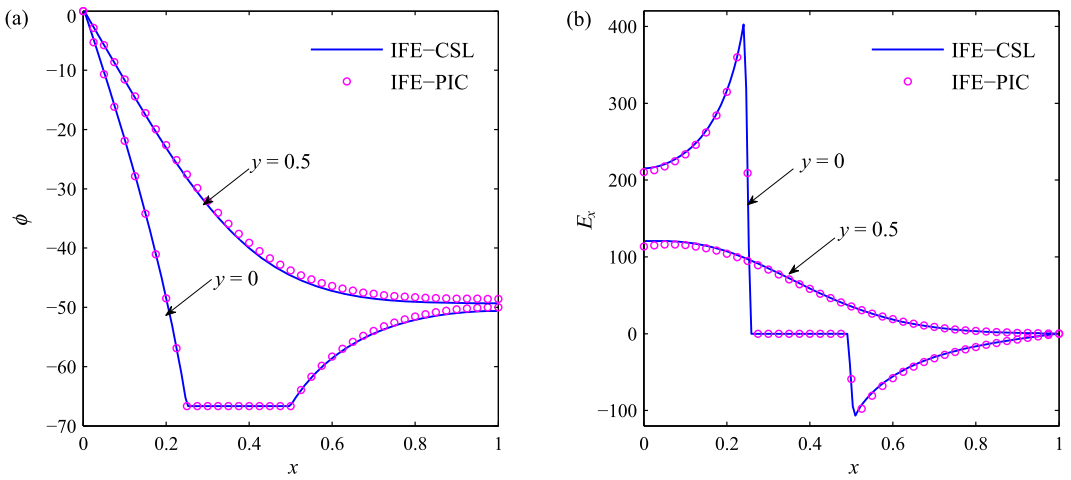

Fig. 13. The plasma electric potential ϕ (a) and electric field E_x (b) at $y = 0$ against the physical space x.

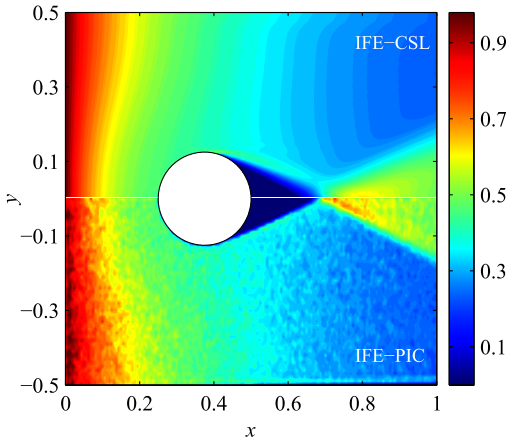

Fig. 14. Contours of the plasma number density.

The above arguments indicate that the proposed IFE-CSL based on the hybrid kinetic model actually captures the interactions of the ion dynamic and complex conductor. Besides, the statistical noise in particle-based methods is essentially eliminated in proposed IFE-CSL, making it useful for investigating small-scale physics and unsteady plasma dynamics involving a small perturbation amplitude and high energy tail.

5. Conclusions

In this paper, coupling the immersed finite element (IFE) method and conservative semi-Lagrangian scheme (CSL) via the charge density based on full kinetic or hybrid kinetic model, we present a noiseless plasma kinetic solver, termed IFE-CSL, for plasma-material interactions. The proposed IFE-CSL enables handling complex interface problems on a Cartesian mesh independent of the interface. The classical plasma sheath is carried out to validate the current IFE-CSL, where numerical results agree well with the analytic solution. Applications of IFE-CSL to plasma sheath with rough wall and plasma past a charged cylinder are also presented to show the capability of IFE-CSL for practical problems of science and engineering interest. Numerical results show that IFE-CSL is free from noise and can accurately capture the interactions of the plasma dynamic and irregular objects based on Cartesian meshes. For these reasons, we expect that the proposed IFE-CSL would be a promising tool for small-scale physics and unsteady plasma dynamics involving complex interface conditions.

Note that current IFE-CSL only requires the interface information and gets rid of regenerating repeatedly the mesh. Therefore, the IFE-CSL can be naturally extended for the plasma simulations involving moving objects as an interesting future work, although the current work mainly presents the results of dielectric objects immersed in a stationary plasma. Besides, further development of current IFE-CSL for electromagnetic plasma simulations will be presented in our future work.

CRediT authorship contribution statement

Hongtao Liu: Conceptualization, Methodology, Software, Validation, Writing – original draft. **Mengyu Chen:** Software, Validation, Writing – original draft. **Xiaofeng Cai:** Methodology, Validation, Writing – review & editing. **Yong Cao:** Funding acquisition, Project administration, Supervision, Validation. **Giovanni Lapenta:** Funding acquisition, Resources, Supervision, Writing – review & editing.

Declaration of competing interest

The authors declared that they have no conflicts of interest to this work. We declare that we do not have any commercial or associative interest that represents a conflict of interest in connection with the work submitted.

Data availability

Data will be made available on request.

Acknowledgements

This work was supported by Shenzhen Technology Projects (ZDSYS201707280904031), China. At KU Leuven, the work was supported by the KU Leuven Bijzonder Onder-zoeksfonds (BOF) under the C1 project TRACESpace, by the European Union's project DEEP-SEA (Grant agreement 955606). Cai was partially supported by National Natural Science Foundation (China) [Grant Number 12201052], the Guangdong Provincial Key Laboratory of Interdisciplinary Research and Application for Data Science, project code 2022B1212010006, and Guangdong Higher Education Upgrading Plan (2021-2025) of "Rushing to the Top, Making Up Shortcomings and Strengthening Special Features" with UIC research grant R0400001-22.

References

[1] F.F. Chen, Introduction to Plasma Physics and Controlled Fusion, vol. 1, Springer, 1984.
[2] F. Filbet, C. Yang, An inverse Lax–Wendroff method for boundary conditions applied to Boltzmann type models, J. Comput. Phys. 245 (2013) 43–61.
[3] C.S. Peskin, Numerical analysis of blood flow in the heart, J. Comput. Phys. 25 (1977) 220–252.
[4] S. Osher, J.A. Sethian, Fronts propagating with curvature-dependent speed: algorithms based on Hamilton-Jacobi formulations, J. Comput. Phys. 79 (1988) 12–49.
[5] T. Lin, Y. Lin, R. Rogers, M.L. Ryan, A rectangular immersed finite element space for interface problems, Adv. Comput. Theory Pract. 7 (2001) 107–114.
[6] Z. Li, T. Lin, X. Wu, New Cartesian grid methods for interface problems using the finite element formulation, Numer. Math. 96 (2003) 61–98.
[7] R. Kafafy, T. Lin, Y. Lin, J. Wang, Three-dimensional immersed finite element methods for electric field simulation in composite materials, Int. J. Numer. Methods Eng. 64 (2005) 940–972.
[8] Y. Chu, D. Han, Y. Cao, X. He, J. Wang, An immersed-finite-element particle-in-cell simulation tool for plasma surface interaction, Int. J. Numer. Anal. Model. 14 (2017).
[9] Y. Cao, Y. Chu, X. He, T. Lin, An iterative immersed finite element method for an electric potential interface problem based on given surface electric quantity, J. Comput. Phys. 281 (2015) 82–95.
[10] J. Bai, Y. Cao, Y. Chu, X. Zhang, An improved immersed finite element particle-in-cell method for plasma simulation, Comput. Math. Appl. 75 (2018) 1887–1899.
[11] H. Cao, Y. Chu, E. Wang, Y. Cao, G. Xia, Z. Zhang, Numerical simulation study on barrel erosion of ion thruster accelerator grid, J. Propuls. Power 31 (2015) 1785–1792.
[12] H. Jian, Y. Chu, H. Cao, Y. Cao, X. He, G. Xia, Three-dimensional ife-pic numerical simulation of background pressure's effect on accelerator grid impingement current for ion optics, Vacuum 116 (2015) 130–138.
[13] H. Cao, Q. Li, K. Shan, Y. Cao, L. Zheng, Effect of preionization on the erosion of the discharge channel wall in a Hall thruster using a kinetic simulation, IEEE Trans. Plasma Sci. 43 (2014) 130–140.
[14] H. Cao, Y. Cao, Y. Chu, X. He, T. Lin, A Huygens immersed-finite-element particle-in-cell method for modeling plasma-surface interactions with moving interface, Commun. Nonlinear Sci. Numer. Simul. 59 (2018) 132–148.
[15] D. Han, P. Wang, X. He, T. Lin, J. Wang, A 3d immersed finite element method with non-homogeneous interface flux jump for applications in particle-in-cell simulations of plasma–lunar surface interactions, J. Comput. Phys. 321 (2016) 965–980.
[16] D. Han, J. Wang, X. He, A nonhomogeneous immersed-finite-element particle-in-cell method for modeling dielectric surface charging in plasmas, IEEE Trans. Plasma Sci. 44 (2016) 1326–1332.
[17] S. Markidis, G. Lapenta, et al., Multi-scale simulations of plasma with iPIC3D, Math. Comput. Simul. 80 (2010) 1509–1519.
[18] G. Lapenta, Particle simulations of space weather, J. Comput. Phys. 231 (2012) 795–821.
[19] G. Lapenta, Exactly energy conserving semi-implicit particle in cell formulation, J. Comput. Phys. 334 (2017) 349–366.
[20] Y. Hu, J. Wang, Expansion of a collisionless hypersonic plasma plume into a vacuum, Phys. Rev. E 98 (2018) 023204.
[21] G. Lapenta, W. Jiang, Implicit temporal discretization and exact energy conservation for particle methods applied to the Poisson–Boltzmann equation, Plasma 1 (2018) 242–258.
[22] K. Xu, J.-C. Huang, A unified gas-kinetic scheme for continuum and rarefied flows, J. Comput. Phys. 229 (2010) 7747–7764.
[23] Z. Guo, K. Xu, R. Wang, Discrete unified gas kinetic scheme for all Knudsen number flows: low-speed isothermal case, Phys. Rev. E 88 (2013) 033305.
[24] H. Liu, Y. Cao, Q. Chen, M. Kong, L. Zheng, A conserved discrete unified gas kinetic scheme for microchannel gas flows in all flow regimes, Comput. Fluids 167 (2018) 313–323.
[25] J. Chen, S. Liu, Y. Wang, C. Zhong, Conserved discrete unified gas-kinetic scheme with unstructured discrete velocity space, Phys. Rev. E 100 (2019) 043305.
[26] T. Chen, X. Wen, L.-P. Wang, Z. Guo, J. Wang, S. Chen, Simulation of three-dimensional compressible decaying isotropic turbulence using a redesigned discrete unified gas kinetic scheme, Phys. Fluids 32 (2020) 125104.

[27] H. Liu, M. Kong, Q. Chen, L. Zheng, Y. Cao, Coupled discrete unified gas kinetic scheme for the thermal compressible flows in all Knudsen number regimes, Phys. Rev. E 98 (2018) 053310.
[28] L. Yang, X. Zhao, C. Shu, Y. Du, Parametric reduced order modeling-based discrete velocity method for simulation of steady rarefied flows, J. Comput. Phys. (2020) 110037.
[29] C. Cui, J. Wang, Grid-based Vlasov simulation of collisionless plasma expansion, Phys. Plasmas 28 (2021) 093510.
[30] E. Camporeale, G.L. Delzanno, B. Bergen, J.D. Moulton, On the velocity space discretization for the Vlasov–Poisson system: comparison between implicit Hermite spectral and particle-in-cell methods, Comput. Phys. Commun. 198 (2016) 47–58.
[31] X. Cai, W. Guo, J.-M. Qiu, A high order semi-Lagrangian discontinuous Galerkin method for Vlasov–Poisson simulations without operator splitting, J. Comput. Phys. 354 (2018) 529–551.
[32] X. Cai, W. Guo, J.-M. Qiu, A high order semi-Lagrangian discontinuous Galerkin method for the two-dimensional incompressible Euler equations and the guiding center Vlasov model without operator splitting, J. Sci. Comput. 79 (2019) 1111–1134.
[33] H. Liu, L. Quan, Q. Chen, S. Zhou, Y. Cao, Discrete unified gas kinetic scheme for electrostatic plasma and its comparison with the particle-in-cell method, Phys. Rev. E 101 (2020) 043307.
[34] H. Liu, F. Shi, J. Wan, X. He, Y. Cao, Discrete unified gas kinetic scheme for a reformulated BGK-Vlasov-Poisson system in all electrostatic plasma regimes, Comput. Phys. Commun. (2020) 107400.
[35] F. Filbet, E. Sonnendrücker, P. Bertrand, Conservative numerical schemes for the Vlasov equation, J. Comput. Phys. 172 (2001) 166–187.
[36] J.-M. Qiu, C.-W. Shu, Positivity preserving semi-Lagrangian discontinuous Galerkin formulation: theoretical analysis and application to the Vlasov–Poisson system, J. Comput. Phys. 230 (2011) 8386–8409.
[37] H. Liu, X. Cai, G. Lapenta, Y. Cao, Conservative semi-Lagrangian kinetic scheme coupled with implicit finite element field solver for multidimensional Vlasov Maxwell system, Commun. Nonlinear Sci. Numer. Simul. 102 (2021) 105941.
[38] T. Xiong, J.-M. Qiu, Z. Xu, A. Christlieb, High order maximum principle preserving semi-Lagrangian finite difference WENO schemes for the Vlasov equation, J. Comput. Phys. 273 (2014) 618–639.
[39] G. Dimarco, L. Pareschi, Numerical methods for kinetic equations, Acta Numer. (2014) 369–520.
[40] S. Tao, H. Zhang, Z. Guo, L.-P. Wang, A combined immersed boundary and discrete unified gas kinetic scheme for particle–fluid flows, J. Comput. Phys. 375 (2018) 498–518.
[41] T. Seta, K. Hayashi, A. Tomiyama, Analytical and numerical studies of the boundary slip in the immersed boundary-thermal lattice Boltzmann method, Int. J. Numer. Methods Fluids 86 (2018) 454–490.
[42] S. Tao, Q. He, B. Chen, F.G. Qin, Y. Lin, A ghost-cell discrete unified gas kinetic scheme for thermal flows with heat flux at curved interface, Int. J. Heat Mass Transf. 162 (2020) 120365.
[43] L.K. Ragta, B. Srinivasan, S.S. Sinha, Unified gas kinetic scheme combined with Cartesian grid method for intermediate Mach numbers, Int. J. Numer. Methods Fluids 85 (2017) 507–524.
[44] S. Tao, L. Wang, Y. Ge, Q. He, Application of half-way approach to discrete unified gas kinetic scheme for simulating pore-scale porous media flows, Comput. Fluids 214 (2021) 104776.
[45] M.A. Lieberman, A.J. Lichtenberg, Principles of Plasma Discharges and Materials Processing, John Wiley & Sons, 2005.
[46] C.-Z. Cheng, G. Knorr, The integration of the Vlasov equation in configuration space, J. Comput. Phys. 22 (1976) 330–351.
[47] X. He, T. Lin, Y. Lin, Approximation capability of a bilinear immersed finite element space, Numer. Methods Partial Differ. Equ. 24 (2008) 1265–1300.
[48] Y. Saad, Iterative Methods for Sparse Linear Systems, SIAM, 2003.
[49] V. Kolobov, R. Arslanbekov, Towards adaptive kinetic-fluid simulations of weakly ionized plasmas, J. Comput. Phys. 231 (2012) 839–869.
[50] K. Hara, K. Hanquist, Test cases for grid-based direct kinetic modeling of plasma flows, Plasma Sources Sci. Technol. 27 (2018) 065004.
[51] A. Christlieb, W. Guo, Y. Jiang, A WENO-based method of lines transpose approach for Vlasov simulations, J. Comput. Phys. 327 (2016) 337–367.
[52] L.P. Rose, Development of 1d particle-in-cell code and simulation of plasma-wall interactions, Master's thesis, The George Washington University, 2014.
[53] L. Brieda, Plasma Simulations by Example, CRC Press, 2019.